Photoionization of N^{3+} and Ar^{8+} in an electron beam ion trap by synchrotron radiation

Photoionization of N³⁺ and Ar⁸⁺ in an electron beam ion trap by synchrotron radiation

M C Simon[1], M Schwarz[1], S W Epp[1,2], C Beilmann[1], B L Schmitt[1], Z Harman[1,3], T M Baumann[1], P H Mokler[1], S Bernitt[1], R Ginzel[1], S G Higgins[1], C H Keitel[1], R Klawitter[1], K Kubiček[1], V Mäckel[1], J Ullrich[1] and J R Crespo López-Urrutia[1]

[1] Max-Planck-Institut für Kernphysik, Saupfercheckweg 1, D-69117 Heidelberg, Germany
[2] Max Planck Advanced Study Group, Center for Free-Electron Laser Science, Luruper Chaussee 149, D-22761 Hamburg, Germany
[3] ExtreMe Matter Institute EMMI, Planckstrasse 1, D-64291 Darmstadt, Germany

E-mail: martin.simon@mpi-hd.mpg.de, crespojr@mpi-hd.mpg.de and zoltan.harman@mpi-hd.mpg.de

Abstract
Photoionization (PI) of multiply and highly charged ions was studied using an electron beam ion trap and synchrotron radiation at the BESSY II electron storage ring. The versatile new method introduced here extends the range of ions accessible for PI investigations beyond current limitations by providing a dense target of ions in arbitrary, i.e. both low and high charge states. Data on near-threshold PI of N³⁺ and Ar⁸⁺ ions, species of astrophysical and fundamental interest, show high resolution and accuracy allowing various theoretical models to be distinguished, and highlight shortcomings of available PI calculations. We compare our experimental data with our new fully relativistic PI calculations within a multiconfiguration Dirac–Fock approach and with other advanced calculations and find generally good agreement; however, detailed examination reveals significant deviations, especially at the threshold region of Ar⁸⁺.

(Some figures in this article are in colour only in the electronic version)

1. Introduction

The interaction of light and matter through photoionization (PI) of atoms and ions is a truly fundamental process and many efforts have led to a large body of experimental and theoretical work for atoms and also for ions in low charge states. Comprehensive databases have been set up, such as the Opacity Project (TOP) [1], the IRON Project [2] and the FERRUM Project [3], which have collected the calculations of international collaborations. Unfortunately, for highly charged ions (HCIs) a multitude of sometimes contradictory predictions have only a scarce foundation of accurate laboratory data until now. The main reason for this status quo is the fact that preparation of HCI targets of sufficient density and stability still presents a serious experimental challenge. Our present work introduces a novel experimental method for precise PI measurements using HCIs having high ionization potentials and charge states which were beyond reach until now. Moreover, we performed new, extended fully relativistic calculations in the multiconfiguration Dirac–Fock (MCDF) frame, which compare well with the present experimental data.

In astrophysics, PI of HCIs has been recently observed in high-resolution x-ray spectra of quasars, which display absorption lines due to the presence of HCIs in the line of sight [4]. Such data have revealed the hitherto only presumed existence of a tenuous warm–hot intergalactic medium, the so-called WHIM [5], comprising a large fraction of baryonic matter in large-scale filaments at temperatures, which are consistent with the now detected abundance of such highly ionized species. First estimates of temperature (0.3–5 million degrees), density (10–100 times the mean baryon density of the

universe) and mass of the medium have been obtained through the analysis of the O^{5+} spectrum [6–11], and quantitative studies have involved O^{6+} and O^{7+} ions. Further abundant HCIs such as C, N, Ne, Ar and Fe in various charge states are expected to contribute to the detected photoabsorption [12, 13]. Other photoionized astrophysical plasmas such as those found in active galactic nuclei (AGNs) and accretion disks had been already known. At present, the identification of absorption lines due to HCIs in astrophysical spectra is based nearly exclusively on theoretical predictions, which have large uncertainties. In general, it can be said that in astrophysical codes [23] the quantitative modelling of PI is still insufficiently taken into account and a more sophisticated theoretical treatment is needed in future modelling.

Beyond the astrophysical relevance, investigations of HCIs provide stringent tests of atomic theory, since relativistic effects, quantum electrodynamic contributions and nuclear size effects grow with high powers of the charge state in those ions. They also offer the possibility of performing systematic studies on electron–electron correlation along isoelectronic and isonuclear sequences, a tool capable of providing deep insights into many-body quantum mechanics. Since direct PI measurements are largely missing for HCIs the study of the time-reversed process to PI, namely photorecombination, using ion storage ring [14–17] and electron beam ion trap (EBIT) [18–22] techniques has given access to valuable data for benchmarking theory through the principle of detailed balance. However, these methods only gave a partial view of PI, and direct measurements are of great importance. The application of synchrotron radiation sources to atomic and condensed matter physics has brought the development of high spectral resolution instrumentation (up to $E/\Delta E \approx 200\,000$) which can in principle overcome the current resolution limitations of ion storage ring and EBIT electron–ion photorecombination experiments. In this context, the PI of low charge ions already constitutes a technique of remarkable accuracy [24]. These points clearly emphasize the need for PI investigations on HCIs to interpret astrophysical spectra and to guide advanced atomic structure calculations.

2. Present status

The broad interest in data on PI of ions has led to the development of sophisticated methods utilizing merged beams (MB), transient plasmas (e.g. dual laser-produced plasma—DLP) and ion traps. Unfortunately, none of the established experimental techniques is capable of accessing truly high charge states, or only with very limited resolution. In fact, only a few measurements exist in which the ionization potential (E_{IP}) of the investigated ion is higher than 150 eV (see figure 1).

In the last decade, the highest accuracy in PI was achieved by the MB method in measurements of mainly singly and multiply charged ions with charge states $q \leqslant 3$ for lighter elements, e.g. [31], $q \leqslant 6$ for Ba [32] and Fe [33], $q \leqslant 7$ for Xe [34] and results with $q \leqslant 9$ have been presented for Ce [35], see figure 1. In those experiments, a beam of ions in the charge state q with a typical area density below 10^7 cm^{-2} is exposed
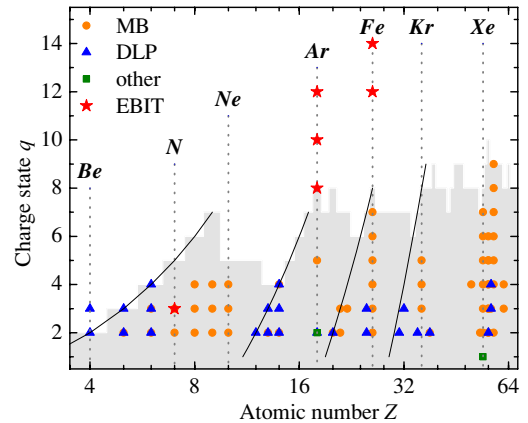

Figure 1. Representative overview of ions in charge states $q \geqslant 2$ for which PI experiments have been performed [25, 26]. The ordinate indicates the charge state q and the abscissa the atomic number Z. Ions investigated by MB (orange circles), DLP (blue triangles) and Penning traps (green squares) [27, 28] are compared to those studied in the course of this work with an EBIT (red stars) [29, 30], in order to illustrate the remarkable extension of the accessible charge states. The grey area marks the charge states for each element having an ionization potential below 150 eV. The black lines indicate closed shell isoelectronic sequences.

to synchrotron radiation. The ionized species, i.e. photoions having the charge state ($q + 1$), is separated downstream and detected (cf review by Kjeldsen [36]). However, for higher charge states, the achievable target ion area density drops severely in ion beams, bringing the photoion signal below the noise level. Higher HCI densities are reached in discharge or laser plasmas (cf review by West [37] and [38–42]). Pulsed radiation sources used as backlighters allow photoabsorption measurements, but separating photoions is impractical. The transient conditions of both plasma and backlighter, as well as of the plasma density gradients, and the simultaneous presence of different ionic species cause large experimental uncertainties.

Only two PI measurements using trapped ions have been reported, both suffering severe density limitations. Ar^{2+} ions stored in a Penning trap were exposed to broadband synchrotron radiation producing K-shell vacancies [27]. Photoions up to Ar^{8+} resulted from the subsequent electron shake-off. Recently, Xe^{+} was photoionized in a Penning trap [28], and the Fourier transform-ion cyclotron resonance method was then applied to extract the photoion signal. Using trapped ions allows for the suppression of undesirable contributions from target ions in metastable states (up to 50% in MB experiments). However, low target area densities of only 10^6 cm^{-2} imply that these techniques will neither lead to significant improvements in sensitivity, nor enable HCI studies.

Here we demonstrate a promising new approach towards PI investigations with ions and HCIs, where high photon flux from a synchrotron irradiates the ions confined in an EBIT. Data on N^{3+} and Ar^{8+} ions show the versatility of this method. All HCIs of astrophysical interest, such as O^{4+} to O^{6+} or Fe^{6+} to Fe^{16+}, as well as those relevant to hot fusion plasmas [43–45] are now accessible. The idea had been discussed already in
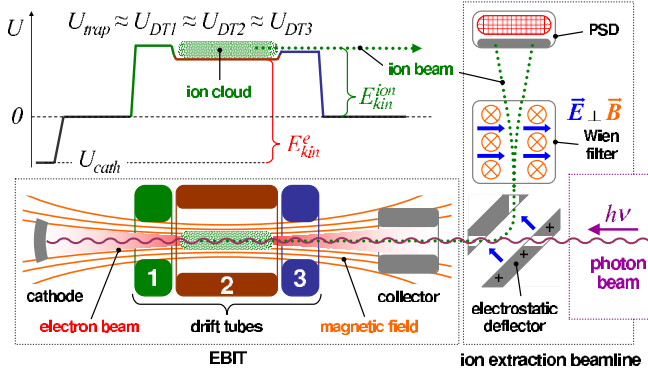
Figure 2. Experimental setup for PI measurements using synchrotron radiation (coming from the right side) and an EBIT (bottom-left box) equipped with an ion extraction (right box). Ions are produced and trapped by a compressed electron beam, forming a cloud with area density $\approx 10^{10}\,\mathrm{cm}^{-2}$, which is axially overlapped with a photon beam. The electron kinetic energy $E_{kin}^e = e \cdot (U_{trap} - U_{cath})$ must stay below the photon energy $h\nu$. The left top graph shows the potential settings in the EBIT. Target ions and photoions are extracted with a kinetic energy of $E_{kin}^{ion} = q \cdot U_{trap}$ (where U_{trap} is characterized by the drift tube potentials U_{DTi}), bent towards a velocity filter separating them by the charge-to-mass ratio (q/m) and counted with a position-sensitive detector (PSD).

1984 by Church *et al* [46], and an apparatus was built by Kravis and co-workers [47–49], but to our knowledge no results on PI of HCIs have been reported so far.

The Be-like N^{3+} ion was chosen for demonstration due to its astrophysical abundance, to test predictions on threshold and resonance energies and their (relative) strengths commonly used for plasma modelling. For argon the situation is quite special: in spite of being of astrophysical relevance, motivating numerous theoretical studies, only a few PI experiments have been conducted on this element so far. Ar^{8+} is a Ne-like system, which is very suitable for this type of experiment, as it can be prepared at relatively high densities. Furthermore, PI investigations of neutral atoms are especially simple on noble gases; hence, Ar^{8+} is located on an isoelectronic [50–53] and isonuclear sequence [27, 54–56] reaching down to the neutral system.

3. Experimental arrangements

As indicated by dotted boxes in figure 2, the setup consists of three main components: the EBIT produces the target ions, the synchrotron provides the required photons and an ion extraction beamline is used for photoion detection. The experimental setup with these components as well as the different applied measuring modes is described in the following.

3.1. Electron beam ion trap

An EBIT generates a dense target of HCIs, well controlled and understood in terms of charge states, their time evolution and spatial distribution [57–59] governed by the electron beam energy $\left(E_{kin}^e\right)$ and current (I_e). The electron beam is accelerated by the potential difference between the cathode

(U_{cath}) and the trap (U_{trap}), which consists of an assembly of ring-shaped electrodes, called drift tubes (DTi, $i = 1, 2, 3$). A strong magnetic field, usually produced by superconducting coils, guides and compresses the electron beam. Atoms or molecules injected into the trap centre are ionized through electron impact ionization (EII). Positively charged particles are radially trapped by the negative space charge of the electron beam, which is directly proportional to I_e and inversely to $\sqrt{E_{kin}^e}$. Potentials applied to the DTs control the axial confinement, forming a cylindrically shaped trapping volume of ≈ 50 mm length and tens to hundreds of micrometres diameter (ion cloud). The trapped ions are further ionized to higher charge states until the ionization potential lies above the electron beam energy. Even higher charge states will only be produced in traces through two-step processes involving long-lived metastable intermediate states.

The control over the charge states is of crucial importance for a PI experiment, where the ion cloud is brought to overlap with a photon beam of energy $h\nu$. By choosing an electron beam energy just sufficient to produce target ions in the charge state q, the detection of ions with charge $(q + 1)$ can be linked to PI:

$$E_{kin}^e \approx e \cdot (U_{trap} - U_{cath}) \leqslant E_{IP}^q \leqslant h\nu. \qquad (1)$$

In principle, a higher electron beam energy beyond the ionization potential could lead to a more efficient population of the target state, but EII by current densities of typically $J_e \approx 10^{21}$ electrons s^{-1} cm^{-2} would completely dominate PI due to the photon flux of $\Phi_\gamma \approx 10^{16}$ photons s^{-1} cm^{-2} and reduce the signal to noise ratio for the photoion:

$$J_e \cdot \sigma_{EII} \gg \Phi_\gamma \cdot \sigma_{PI}. \qquad (2)$$

A rough estimate on the target ion area density can be derived by assuming that the total charge of the ion cloud amounts approximately to the total charge of the electron beam within the trap volume:

$$\underbrace{I_e\, l\, \sqrt{\frac{m_e}{2e\Delta U}}}_{\text{total electron charge}} \approx \underbrace{e \sum_{Z} \sum_{q=1}^{q_{max}(Z)} q \cdot N_{q,Z}}_{\text{total ion charge}}, \qquad (3)$$

where l stands for the length of the ion cloud, m_e for the electron mass, e for the elementary charge, ΔU for the electron beam accelerating potential ($\approx U_{trap} - U_{cath}$) and $N_{q,Z}$ for the number of ions of a certain element Z in the charge state q. By assuming a uniform charge state distribution $\left(N_1 = N_2 = \cdots = N_{q_{max}}\right)$, a simple expression replaces the inner sum in (3) and an estimate on the involved ion area density $\tilde{\rho}$ can be obtained:

$$\sum_{q=1}^{q_{max}} q \cdot N_q = N_{q_{max}} \frac{q_{max}(q_{max} + 1)}{2} \approx N_{q_{max}} \frac{q_{max}^2}{2}, \qquad (4)$$

$$\tilde{\rho}(Z, q_{max}) = \frac{N_{q_{max}}}{A} \approx f \frac{4}{d_{IC}^2 \pi} \frac{I_e l}{e q_{max}^2} \sqrt{\frac{2m_e}{e\Delta U}}, \qquad (5)$$

where $\tilde{\rho}$ is the target ion area density, d_{IC} is a measure for the ion cloud diameter (typically $250\,\mu$m) and f is a *charge fraction factor* accounting for charge contributions by other elements, degree of electron charge compensation and the

simplistic assumption of a uniform charge state distribution. An estimate within an order of magnitude should be possible even if f introduces a certain degree of freedom. Typical values for $\tilde{\rho}$ are $10^9\,\mathrm{cm}^{-2}$ to $10^{10}\,\mathrm{cm}^{-2}$. These estimates are also supported by our recent quantitative analysis of VUV spectroscopic EBIT data on Fe ions in [60, 61]. At this point it should be emphasized once more that this ion area density represents an increase of three to four orders of magnitude, when compared to an ion beam typically utilized in MB experiments. Therefore, it is advantageous to directly expose the trapped ion cloud of an EBIT to synchrotron radiation, instead of using extracted HCIs, even if such a trapped target is an ensemble of ions in different charge states. Laser-produced plasmas, while reaching much higher densities, survive for only nanoseconds to microseconds, whereas the EBIT ion cloud can be sustained for periods of time from fractions of a second to hours.

3.2. Photon source

The work was performed at the BESSY II electron storage ring in Berlin with the transportable FLASH-EBIT, developed at the Max-Planck-Institut für Kernphysik (Heidelberg) for experiments at modern light sources. Using this device, resonant laser spectroscopy was recently extended into the soft x-ray region at the Free electron LASer in Hamburg (FLASH) [62]. That work on resonant excitation of the $^2S_{1/2}$–$^2P_{1/2}$ transition in Li-like Fe^{23+} at 49 eV also suggested potential applications to PI studies, since EBITs can produce nearly any ionic system of interest. During two campaigns at BESSY II, the FLASH-EBIT was installed at two undulator beamlines covering different energy regions. N^{3+}, having an ionization threshold energy of $E_{IP}^{N3+} \approx 77$ eV, was investigated at the beamline U125/2-SGM [63], which is designed for photon energies in the range from 40 eV to 180 eV, and equipped with a monochromator having a resolving power $E/\Delta E$ greater than 50 000. Ar^{8+}, with a significantly higher ionization potential of $E_{IP}^{Ar8+} \approx 422$ eV, was studied at the beamline U49/2-PGM1 [64–66], supplying photons at energies from 85 eV to 1600 eV. Both beamlines achieve maximal fluxes of 10^{13} photons s^{-1} (at a 100 mA ring current and at a bandwidth of 0.1%). The ion cloud was brought to overlap with the photon beam with the aid of a scintillation crystal, which can be moved in and out of the trap. The fluorescence light induced by the photon beam or the electron beam (as a proxy for the position of the ion cloud) was imaged on a CCD detector. More details on this system can be found in [29].

3.3. Ion extraction

With an EBIT, detection of photoelectrons or photoabsorption is currently not an option for obvious technical reasons (strong electron beam, weak total photon absorption, trap geometry). Hence, the observation of the PI process is bound to the photoion signal. To analyse the trap contents, ions extracted from the trap through the collector were detected (see figure 2). The extracted ion beam was bent off the photon beam axis after passing through the collector by an electrostatic 90° deflector. Subsequently, the ions were separated according to
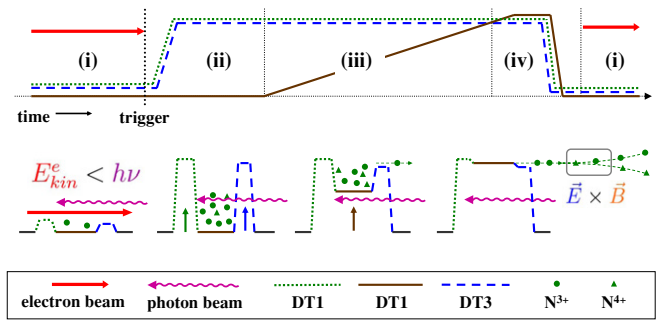

Figure 3. Measurement cycle (6 s long) for PI of N^{3+} ions (green circles). The electron beam energy stays below the EII-production threshold (77 eV) for N^{4+} (green triangles). Target ion production and photoion extraction are performed sequentially in four phases: (i) production of N^{3+} target ions with the electron beam on, and turning off the electron beam at the end, (ii) fixing the ion cloud by raising the confining potentials, (iii) slow ion extraction by reducing the trap depth and (iv) emptying the trap totally before resetting. Timing of DT potentials is shown in the upper panel (DT1: green dotted line, DT2: brown full line, DT3: blue dashed line); axial trap configurations are shown below. Cycles are triggered by the monochromator control software.

their charge-to-mass ratio (q/m) by means of a Wien velocity filter. The electric and magnetic crossed fields of the Wien filter were chosen such that target ions and photoions impinge upon disparate regions of a position sensitive detector (PSD) at highest spatial resolution. High sensitivity can be achieved with this setup, as the PSD (consisting of a micro channel plate and a delay line anode) detects individual ions with an efficiency close to 100% and low background noise.

The ion extraction can be performed in a continuous or pulsed mode depending on the ionization potential of the ion under study. In the continuous mode the potentials of the DTs (see top left in figure 2) are chosen to form a shallow trap, allowing ions which overcome the trap barrier to escape (evaporate). Starting from a deep trap with no evaporative losses and increasing the potential on the central electrode DT2 until the ions are pushed over the trap barrier leads to the pulsed mode (compare to figure 3). In both cases DT3 is kept at a slightly lower potential than DT1 to guarantee that practically all ions leave the trap towards the collector. The trap potential U_{trap} (and the ion charge state q) determines the kinetic energy of the ions.

Typically, low ion currents in the continuous extraction mode are suitable for counting on the PSD, while the pulsed mode requires a careful slow depletion of the trap in order not to saturate the detector. The sensitivity depends on the ion extraction efficiency. In general, ion transport losses are higher at low ion beam energy. Hence, a minimal acceleration voltage is required, setting a lower bound for the trap potential of a few hundred volts. For target ions in a low ionization stage this contradicts the demand expressed by (1). In this case, the target ion preparation (using a low trap potential) has to be separated in time from the photoion detection, consequently performed by a pulsed extraction (at a high trap potential). Data on N^{3+} have been obtained in such a cyclic measurement procedure, which is described in detail below. We achieved efficient ion extraction with

a trap potential of only $U_{\text{trap}} = 300\,\text{V}$. Therefore, Ar^{8+} with $E_{\text{IP}}^{\text{Ar}8+} \approx 422\,\text{eV}$ could be measured in the preferable continuous mode. EBIT-based measurements on ions with a low ionization potential are especially challenging. Hence, the cyclic (or pulsed) measurement procedure for N^{3+} ($E_{\text{IP}}^{\text{N}3+} \approx 77\,\text{eV}$) shall be treated first.

3.4. Cyclic measurement mode for low ionization potentials: N^{3+} ions

We applied a cyclic measurement mode with a total duration of 6 s and four different phases, as depicted in figure 3. During phase (i), N^{3+} ions were generated abundantly, with the cathode biased to only $U_{\text{cath}} = -50\,\text{V}$ and DT2 set to ground potential $U_{\text{DT2}} = 0\,\text{V}$ to stay well below the ionization threshold to produce N^{4+} ions. The electron beam current under these conditions was $\approx 2\,\text{mA}$. Inserting these values into (5) yields an N^{3+} area density of $2 \times 10^{10}\,\text{cm}^{-2}$, where a charge fraction factor of $f = 0.3$ was assumed. After about 3.5 s, the electron beam was turned off, while the photon beam was always on. Without the strong negative space charge of the electron beam the radial confinement only relies on the magnetic field. During this so-called EBIT magnetic trapping mode [67], which is basically equivalent to a Penning trap, the ion cloud diameter increases and the ion density is reduced by approximately one order of magnitude. In phase (ii), lasting about 0.5 s, the confining DTs (DT1 and DT3) were ramped up, while the central DT2 was kept at ground potential to eliminate evaporative axial ion losses. During phase (iii), the DT2 potential was slowly raised over about 1 s to empty the trap gradually (pulsed extraction), in order to prevent an overload of the ion-counting PSD. Finally, in phase (iv) during about 1 s all remaining ions were expelled, and the DT potentials were reset. Then, the electron beam was switched on again, turning back to phase (i) to start a new cycle with an incremented photon beam energy.

Further objectives that also demand a cyclic measuring procedure consisting of various phases are for instance the suppression of target ions in metastable states [28] or the variation of the interaction time in order to determine absolute cross sections [30]. In fact, comparing our N^{3+} data with results from MB experiments [68] one can see a reduced contribution from metastable states, which will be discussed in more detail below. The demonstration of an absolute cross-section measurement performed on Fe^{14+} is described elsewhere [30].

3.5. Continuous measurement mode for high ionization potentials: Ar^{8+} ions

In the continuous measurement all the EBIT parameters were kept constant while the photon energy is scanned. Here, a higher target ion area density is maintained by the electron beam throughout the measurement. Moreover, continuous ion extraction enhances evaporative cooling of the trapped ions [59], thus increasing the achievable resolution by reducing Doppler broadening, and can also have further positive effects on the ion target density by concentrating the

trapping volume [57]. Furthermore, unavoidable depopulation of the photoionized species through electron capture or charge exchange is less critical in the continuous mode. Finally, statistical considerations make continuous extraction more favourable than a pulsed one. Cyclic procedures induce more fluctuations in the number of target ions, beam transport, etc, than steady-state conditions, and thus require longer acquisition times to achieve a good statistical quality. Nonetheless, since the reproducibility of the target preparation was good, by normalizing the photoion to the target ion signal a large suppression of those fluctuations could be achieved for both measuring modes.

3.6. Photon energy calibration

Photoabsorption by N_2-molecules in a conventional gas cell at a photon energy of $\approx 400\,\text{eV}$ was used to calibrate the Ar^{8+} data. The uncertainty of the N_2 calibration is roughly 100 meV, and constitutes the main error source in our results for the resonance energies.

Data on N^{3+} were calibrated by injecting an atomic He beam into the trap centre with the electron beam switched off. The DTs were set to positive voltages similar to phase (iv) in figure 3. Photoions were extracted and autoionizing resonances were recorded and identified [50]. This technique is based on photoion detection, which is more sensitive than conventional photoabsorption, and only uses the existing setup as shown in figure 2. We achieved a calibration accuracy of 8 meV, the limiting factor being the chosen monochromator slit width. More details on the so-called photon beam ion source (PhoBIS) calibration mode can be found elsewhere [29, 69]. Generally, He-like systems are very appropriate for calibration procedures, as precise theory is available and, in contrast to even more precisely calculated H-like systems, PI resonances can be observed. An additional advantage of He-like systems is that EBITs have the best performance when producing closed shell ions, and could therefore help establishing new calibration standards at high photon energies.

4. Theory

Simulated PI spectra have been calculated by various models, see e.g. the works [1–3, 70] and references therein. We have calculated for the systems studied here the resonance energies, widths and strengths within a fully relativistic large-scale MCDF method similar to [71, 72] and have compared the results with our experimental data on N^{3+} and Ar^{8+} ions.

The cross section for a given resonant photoionization channel, including quantum interference with the direct photoionization process, can be written as a function of the photon energy $\hbar\omega$ as:

$$\sigma_{i \to d \to f}^{\text{PI}}(\hbar\omega) = S_{i \to d \to f} \frac{2}{\Gamma_d \pi} \frac{1 - 1/q_{\text{F}}^2 + 2\epsilon/q_{\text{F}}}{1 + \epsilon^2}, \quad (6)$$

with the resonance strength $S_{i \to d \to f}$ and the unitless energy ϵ given by:

$$S_{i \to d \to f} = \frac{2\pi^2 c^2 \hbar^4}{(\hbar\omega)^2} \frac{A_{i \to d}^{re} A_{d \to f}^a}{\Gamma_d},$$

$$\epsilon = 2(\hbar\omega + E_i - E_d)/\Gamma_d, \quad (7)$$

and q_F is the Fano asymmetry parameter [73]. Here, i is the initial state (Be- or Ne-like) of the ion. The index d denotes quantities related to the autoionizing state formed by photoabsorption. This intermediate state then decays via autoionization to the final state f. $A_{i \to d}^{re}$ stands for the one-photon radiative excitation rate (transition probability per unit time) and $A_{d \to f}^{a}$ is the autoionization (Auger) rate of the excited resonant state. Γ_d denotes the total natural width of the resonant state, given as the sum of the radiative and autoionization widths: $\Gamma_d = \hbar \left(A_d^r + A_d^a \right)$, where A_d^r and A_d^a are the corresponding decay rates summed over all possible decay channels. A shift of the transition energy ($E_{res} = E_d - E_i$), caused by the coupling to the electronic continuum [73], is included in our definition of E_d. Interference with direct PI may change the line profile and the position of the maximal cross section but not the resonance energy. Our calculated resonance energies and strengths can be compared to experimental data by fitting the function in equation (6) to the measured spectra. When interference with the direct PI channel can be neglected, i.e. $q_F \to \infty$, the energy dependence of the cross section approaches a symmetric Lorentzian line profile:

$$\sigma_{i \to d \to f}^{PI,symm.}(\hbar\omega) = S_{i \to d \to f} \frac{\Gamma_d/(2\pi)}{(\hbar\omega + E_i - E_d)^2 + \frac{\Gamma_d^2}{4}}. \quad (8)$$

We calculate the bound state functions involved in the transition rates and the corresponding level energies E_i and E_d in the framework of the MCDF method [74, 75] as in [71]. In this scheme, the many-electron atomic state function (ASF) is given as a linear superposition of configuration state functions (CSFs) sharing common total angular momentum (J), magnetic (M) and parity (P) quantum numbers:

$$|\text{ASF}; PJM\rangle = \sum_{k=1}^{n_c} c_k |\text{CSF}_k; PJM\rangle. \quad (9)$$

The CSFs are constructed as jj-coupled N-particle Slater determinants of one-electron wavefunctions. In equation (9), a CSF is specified by the orbital occupation and the coupling of subshell angular momenta. The number of CSFs is denoted by n_c. As an example, in the calculation of the bound states involved in the PI of Ne-like Ar we take into account relevant configurations which can be constructed from the dominant one by single- and double-orbital substitutions, resulting typically in hundreds of CSFs. Such an extensive calculation is necessary as relativistic correlation contributions amount to as much as 6 eV to 8 eV, while the experimental accuracy is on the 0.1 eV level. The contribution of the Breit interaction amounts to 3.3 eV to 3.4 eV for the levels involved. The single-electron one-loop quantum electrodynamic (QED) radiative corrections of typically 2.6 eV have also been included, and QED screening corrections were approximated to be around 0.2 eV by a rescaling of the single-electron values. Mass shift effects are on the order of 0.2 eV.

The continuum electron wavefunctions entering the Auger rates $A_{d \to f}^{a}$ are calculated numerically by solving the radial Dirac equation with the screening potential induced by the bound (frozen) electrons, with a method similar to that applied in [76]. In general, within our model we expect typically
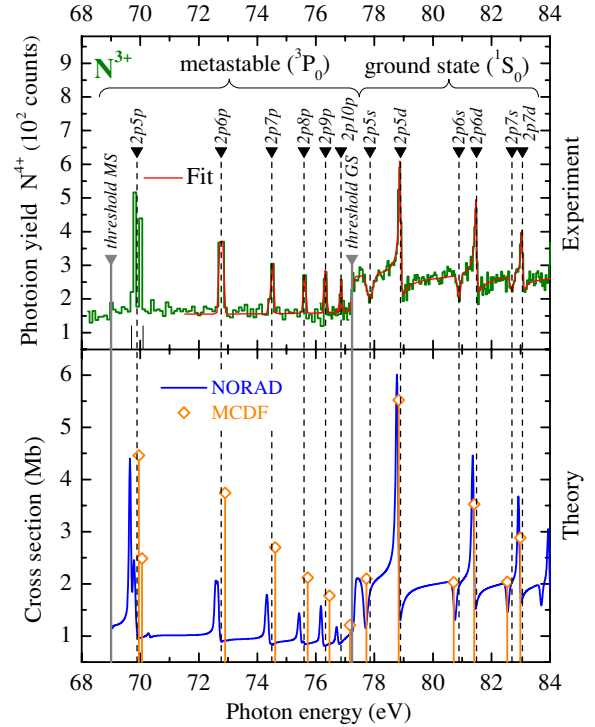

Figure 4. Top: overview spectrum for PI of N^{3+} ions. Counts of N^{4+} ions are plotted versus photon energy (green histogram). Structures are due to autoionizing intermediate states (labels) excited from the ground state (GS) and metastable states (MS) of N^{3+}. Data are normalized to N^{3+} counts and photon flux. Peaks are fitted with Fano or Gaussian profiles (red line). The step size is 100 meV in the range of MS structures and 40 meV in the range of GS structures. Bottom: comparison with available theory by NORAD (blue line) and our MCDF calculations (orange diamonds with drop lines) show good agreement.

an accuracy of 0.3 eV for the resonance energy and 20% for the cross section. Within these uncertainties QED and other subtle effects contribute already noticeably to the resonance positions.

5. Results and discussion

5.1. Photoionization of N^{3+}

The top of figure 4 shows an overview spectrum for PI of the $1s^2 2s^2 \, ^1S_0$ ground state (GS) and the $1s^2 2s 2p \, ^3P_0$ metastable states (MS) of Be-like N^{3+} ions in the range from 68 eV to 84 eV. Data for GS and MS were taken in two individual runs with 40 meV and 100 meV step size, respectively. The observed structures correspond to doubly excited autoionizing intermediate states. Cross sections starting from MS $2s\,2p$ are larger, as a single E1 transition $2s$–nl leads to a doubly excited state, while otherwise two 2s electrons have to be excited through a forbidden transition from the GS $2s^2$ in order to populate the $2p\,ns$ or $2p\,nd$ series of N^{3+}. However, MS and GS resonances appear with similar heights in our measurement, indicating that only a small part of N^{3+} target ions is in the metastable $^3P_0$ state. Comparing the heights of the two ionization edges supports this interpretation. The labels in the plot indicate the doubly

Table 1. Photoionization edges (E) and resonance energies (2p *n*l) fitted with Fano (F) and Gaussian (G) profiles from this work (experiment) compared with merged beam (MB) results from [68] (B), [24] (M—upper two lines), and calculations from this work (MCDF), TOP [1, 80], NIST data [81], as well as Cowan Atomic Structure Code [82, 83]. Values are given in eV.

Transition		This work Experiment	MB, exp.		This work MCDF	TOP	NIST	CATS
MS–2s ∞	E	69.0(2)	69.13	(B)	68.85	68.97	–	69.48
MS–2p 5p $^3D_1$	G	69.805(8)	69.818(3)	(M)	69.95	69.655	69.810	70.106
MS–2p 5p $^3P_1$	G	69.984(8)	70.000(3)	(M)	70.06	69.909	70.001	70.328
MS–2p 5p	G	69.89(5)	69.85(5)	(B)	69.99	69.782	69.906	70.19
MS–2p 6p	G	72.77(5)	72.75(5)	(B)	72.90	72.670	72.790	73.10
MS–2p 7p	G	74.49(5)	74.45(5)	(B)	74.61	74.388	74.503	74.83
MS–2p 8p	G	75.60(5)	75.59(5)	(B)	75.72	75.492	75.621	75.93
MS–2p 9p	G	76.33(5)	76.31(5)	(B)	76.47	76.244	76.364	76.69
MS–2p 10p	G	76.86(5)	76.85(5)	(B)	77.17	76.778	78.881	77.22
GS–2s ∞	E	77.23(5)	–		77.18	77.47	–	75.92
GS–2p 5s	G	77.85(2)	77.72(5)	(B)	77.73	77.93	77.930	76.1
GS–2p 5d	F	78.89(2)	78.88(5)	(B)	78.83	78.40	78.912	77.0
GS–2p 6s	G	80.89(3)	–		80.71	80.81	–	79.3
GS–2p 6d	F	81.49(2)	81.49(5)	(B)	81.41	81.18	81.506	79.8
GS–2p 7s	G	82.70(5)	–		82.54	82.63	–	81.1
GS–2p 7d	F	83.06(3)	–		82.99	82.84	83.080	81.4

excited states 2p *n*l. Counts of N^{4+} photoions for each trap dump were normalized to the corresponding counts of N^{3+} ions and to the photon flux, which was monitored by measuring the photocurrent emitted from a highly transparent gold grid behind the monochromator slit. Fano profiles [73] with Fano parameters around $q_F = -2.3 \pm 0.5$ were fit when the resolution and statistical significance were sufficient (the three 2p*n*d resonances); otherwise Gaussian profiles were used ($q_F \rightarrow \infty$). For the 2p*n*s series the Gaussian profiles are inverted, indicating very small Fano parameters ($q_F \approx 0$). For $q_F = \infty$ or $q_F = 0$ the resonance energy coincides with the maximal cross section.

Predictions taken from the Nahar Ohio State University Radiative Atomic Database (NORAD) [77, 78] are plotted on the bottom of figure 4 after convolution with a Gaussian profile (FWHM = 75 meV) to account for experimental broadening. Generally, good agreement with the experimental results in relative strengths as well as line profiles is found when adding tabulated values of the GS and MS cross sections with same weights. However, this contradicts the experimental finding that the majority of the target ions are in the GS. Furthermore, an overall energy shift of ≈150 meV towards lower photon energies is clearly visible. Predicted resonance energies of our MCDF calculations are plotted as vertical orange lines with the corresponding diamond giving the cross sections on resonance as they would appear after convolution with an experimental broadening of 75 meV (FWHM). In contrast to NORAD values, the weights for MS and GS have not been chosen equal here. Only 25% of the target ions are assumed to be in the excited $^3P_0$ state, which is in better agreement with our experimental results. In order to account for direct PI and improve comparability to NORAD, resonances excited from MS and GS N^{3+} have been increased by 1 Mb and 2 Mb, respectively. For the resonance energies, good agreement is found especially for the GS excitation. For MS excitation, all the resonance positions shift to slightly higher energies,
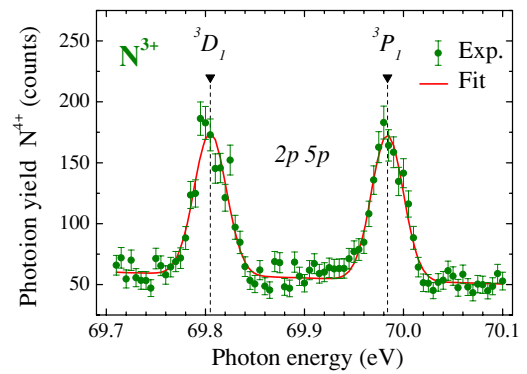

Figure 5. Photoionization of N^{3+} ions in metastable states (green dots). The 2p 5p MS resonance doublet with a 5 meV step size and resolution ≈35 meV (FWHM). The exit slit of the beamline U125/2-SGM was set to 250 μm. Error bars only account for statistical (counting) uncertainties. Resonance energies are extracted by Gaussian fits (red curve) and indicated by dashed drop lines.

indicating a corresponding stronger binding of the MS state. In figure 5 the region around 69.9 eV reveals the doublet structure of the MS 2p 5p resonances. The data were obtained in only 1 h of acquisition time, proving the high sensitivity of our method. Due to time constraints, a resolution of 35 meV was chosen. A high accuracy measurement by Müller *et al* [24] achieved a remarkable resolution of 3.3 meV (FWHM) on the same features, in narrow scans each encompassing one of the lines. For the whole range 68 eV to 88 eV, data with a 40 meV resolution have been preliminarily reported by the same group [24, 79]. The absolute precision of our first demonstration measurement is within a factor of 3 of those results. Table 1 lists our results and compares them to those of MB experiments by Bizau *et al* [68] and, for the 2p 5p $^3P_0$ resonance by Müller *et al* [24], as well as with predictions partially not shown in figure 4 (TOP: *R*-matrix calculation from TOPbase [1, 80], compilation of NIST [81], online calculations from CATS:

Cowan Atomic Structure Code [82, 83]). Excellent agreement between the experimental values of Müller on the 10 meV level can be stated. Our data also agree well (within their larger error bars) with the results of Bizau. In one case, their former identification of the GS $1s^2\, 2p\, 5s$ resonance seems questionable. The thresholds for direct PI of N^{3+} in its GS and MS (mean value) were also determined. Compared to MB experiments, where GS and MS species are nearly equally populated, the MS fraction is considerably suppressed by our cyclic measurement technique. The ratio of the excitation rate of $^3P_{0,1,2}$ by the electron beam to the spontaneous decay rate, combined with the collisional quenching rate, determines the strength of the observed resonances excited in phase (i). During phases (ii) and (iii) the spontaneous decay of the short-lived MS $^3P_{1,2}$ to the GS (below 1 ms lifetime) reduces their contribution.

    R-matrix calculations collected in TOP neglect relativistic effects and use only a very reduced number of levels in the N^{3+} case. These values should not be used any more, as more accurate and elaborate calculations are available, most notably NORAD [77, 78]. The *R*-matrix calculations shown by Müller [24, 79] (values not given here) for MS $2p\, 5p\, ^3P_0$, using a larger set of levels and employing relativistic corrections, achieve the closest agreement with their and our measured data. Resonance energies compiled in the NIST database [81], with recommended values based in part on experiment, seem reliable, but no PI cross sections are given there. Our fully relativistic MCDF calculations yield resonance energies in good agreement with the experiment, even though they are expected to show their real merits especially for heavier systems at higher charge states and photon energies.

5.2. Photoionization of Ar^{8+}

Data on Ar^{8+} were acquired in the continuous measurement mode. An electron beam with an energy of 400 eV ($U_{\text{trap}} = 300\,\text{V}$, $U_{\text{cath}} = -100\,\text{V}$) and a current of 8 mA was steadily maintained. Ions with closed shells like Ar^{8+} can be prepared in very high abundance as the electron beam energy can be adjusted well above the ionization potential of the last open-shell electron ($E_{\text{IP}}^{Ar^{7+}} \approx 143\,\text{eV}$) without having enough energy to promote an electron of the closed shell to the continuum ($E_{\text{IP}}^{Ar^{8+}} \approx 422\,\text{eV}$). This makes it possible to achieve a charge state distribution having its maximum at the highest charge state, i.e. Ar^{8+}. Therefore, estimating the area density based on (5) with a charge fraction factor $f = 1$ seems realistic and yields 1.3×10^{10} ions cm^{-2}. An overview spectrum for Ar^{8+}, including the threshold and near-threshold resonances, is shown in figure 6. The resonances belong to the 2s (2p^6) np Rydberg series (labels in the plot omit the full 2p subshell). Counts of Ar^{9+} ions below the threshold energy are assigned to EII of Ar^{8+} in excited metastable states. The experimental photon energies show calibration uncertainties of approximately 100 meV. On the bottom of figure 6 three calculations are shown for comparison. Values from TOP have been convoluted with a Gaussian profile of FWHM ≈ 300 meV. Like in the plot for N^{3+} our MCDF calculations are indicated by orange drop lines with diamonds giving the cross sections
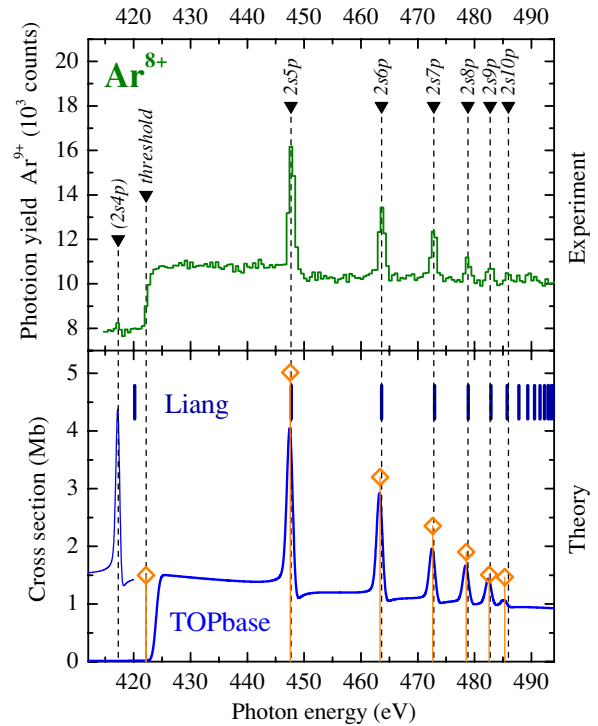

Figure 6. Top: overview PI spectrum on Ar^{8+} in the range from 415 to 495 eV, obtained by counting Ar^{9+} photoions (green histogram) in a continuous extraction mode. Counts of Ar^{9+} below the threshold are interpreted as EII of Ar^{8+} target ions in metastable states. Labelled vertical lines indicate experimental threshold energy and resonance energies of the 2s np Rydberg series. Absolute photon energy calibration with an accuracy of 100 meV is based on photoabsorption by N_2-molecules in a gas cell. Bottom: comparison to our MCDF calculations (orange diamonds with drop lines) as well as available theoretical predictions by TOP [1] (blue line) and Liang *et al* [84] (blue vertical markers). In spite of the threshold region good agreement can be stated. Deviations for resonance energies are on the order of ≈ 300 meV while at the threshold a mismatch of a few eV appears.

(here a broadening of 800 meV was applied). Liang recently presented resonance energies without giving cross sections indicated as blue vertical markers.

    A high-resolution measurement on the first resonance, taken with a 2 h acquisition time and a step size of 5 meV, is depicted in figure 7. The width of the exit slit for the photon beam was set to 15 μm, corresponding to a nominal resolution of $E/\Delta E = 15\,000$ (bandwidth: $< 0.01\%$). The asymmetric shape of the resonance is clearly visible and shows good agreement with TOP predictions (full blue line) after a shift of 145 meV and convolution with a Gaussian profile (FWHM $= 88$ meV). Additionally, a fit of a Fano profile convoluted with an experimental broadening was applied (dashed red line), which yields a resolution of $E/\Delta E \approx 5000$ for this high precision measurement. An asymmetry parameter of $q_F = -6 \pm 1$ and a Fano width $\Gamma = 30 \pm 5$ meV have been obtained by the fitting procedure.

    In table 2 experimental data are compared to our MCDF calculations and to the predictions found in TOP [1], at NIST [81], as well as to online CATS calculations [82, 83], and to recent predictions by Liang *et al* [84]. The values

Table 2. Photoionization edges (E) and resonance energies (2s *n*p) fitted with Fano (F) and Gaussian (G) profiles from this work (experiment) compared with calculations from this work (MCDF), TOP [1, 80], NIST data [81], Cowan Atomic Structure Code (CATS) [82, 83], as well as *relative* values by Liang *et al* [84]. Values are given in eV.

| Transition		This work Experiment	This work MCDF	TOP	NIST	CATS	Liang
2p–∞	E	422.20(12)	422.14(30)	423.953	422.54	422.15	*420.197*
2s–5p	F	447.71(10)	447.54(30)	447.56	–	449.90	*447.71*
2s–6p	G	463.62(12)	463.35(30)	463.34	–	465.76	*463.61*
2s–7p	G	472.80(15)	472.63(30)	472.61	–	475.06	*472.92*
2s–8p	G	478.82(15)	478.53(30)	478.51	–	480.98	*478.85*
2s–9p	G	482.76(18)	482.58(30)	482.50	–	484.98	*482.86*
2s–10p	G	485.94(30)	485.33(30)	485.32	–	487.81	*485.69*
2s–∞	–	*497.80(40)*	–	–	497.44	499.47	*497.39*
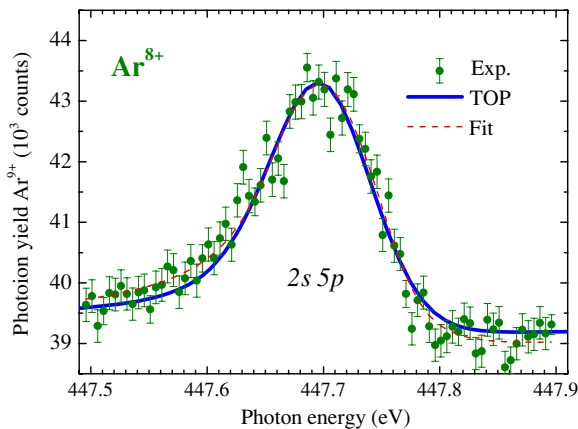
Figure 7. Detailed scan over the 2s 5p resonance with a step size of 5 meV. Counts of Ar^{9+} are plotted versus photon energy (green dots), error bars only include counting statistical uncertainties. TOP calculations (full blue line) are shifted by 145 meV. The fit curve (dashed red line) is a convolution of a Fano profile ($q_F = -6 \pm 1$ and a Fano width $\Gamma = 30 \pm 5$ meV) with an experimental broadening of 88 meV.

from TOP show overall good agreement, but the resonance energies given there are generally too low (≈ 250 meV). The ionization threshold energy, however, is given at 423.95 eV, which is 1.75 eV higher. Moreover, TOP gives values for the 2s 4p resonance with a Fano profile at 417.3 eV, reflecting the theoretical uncertainty, whether this resonance contributes to PI cross sections or not. NIST values were found for the 2p and 2s ionization edge and deviate nearly by 2 eV. CATS resonance energies are available online and calculated rapidly on demand, explaining larger deviations. A shift to higher values of about 2 eV appears for all resonances; therefore, the very good agreement of the ionization edge is probably a coincidence. Recent calculations by Liang [84] using Breit–Pauli Hamiltonian within the *R*-matrix theory show deviations from the data too. There, only resonance energies relative to the threshold are given. For comparison we shifted the energy scale such that resonance energies best reproduce the experimental findings. Applying this shift, the threshold is mispredicted by 2.02 eV. The relative agreement within the Rydberg series between our experiment and Liang is at the 130 meV level.

Experimental data of other Ne-like systems for comparison of PI resonances of the 2s (2p^6) *n*p Rydberg series

only exist for the first three representatives of this isoelectronic sequence (atomic Ne, Na$^+$, Mg^{2+}) and were published by Kennedy *et al* [52]. The first autoionizing resonance is 2s 3p for all three systems and dominates the PI spectra. Fano widths, asymmetry parameters (q_F) and series limits have been extracted for this resonance and can be compared to our values obtained by a fit to the first autoionizing resonance (2s 5p) of Ar^{8+} (see figure 7). The most extensive experimental study on the Ne-like sequence is given by Chakraborty *et al* [51] and reaches up to Si^{4+}. Special attention is drawn to the threshold region, where anomalous behaviour (extremely low direct PI cross sections) was predicted for Si^{4+}. For this charge state the 2s 3p resonance lies very close to the 2s^2 2p^6–2s^2 2p^5 ionization limit. The dual laser plasma (DLP) technique equipped with a photoelectric detection system was applied; hence, photoabsorption was recorded rather than PI. Calculations predict the 2s 3p resonance to lie below the threshold, but the experiment showed an asymmetric Fano profile, indicating interference with direct PI. This was explained as a technical feature of the DLP method, where plasma microfields lower the ionization limit and lead to forced autoionization. Recently, Bizau *et al* [53] performed MB experiments on Si^{4+} in the range from 110 eV to 184 eV at two MB facilities and clearly showed that the 2s 3p resonance does not contribute to PI of that ion. However, the accuracy was not high enough to test the predicted anomalous behaviour. Furthermore, results for the threshold region of different theoretical methods are compared and disagree significantly, as the given threshold energies vary by several eV. The situation for Ar^{8+} is similar. Here, the 2s 4p resonance energy lies close to the ionization threshold. Predictions for E_{IP} scatter by ≈ 3 eV (see figure 2). Inconclusive theoretical predictions, for example in the threshold region of Si^{4+} and Ar^{8+}, corroborate the need for decisive and benchmarking experiments to solve such open questions and guide theory.

6. Summary and outlook

Results of the photoionization of N^{3+} and Ar^{8+} have been obtained with a new experimental method suitable for arbitrary charge states. The ions stored in an EBIT were directly exposed to synchrotron radiation. A high target area density of approximately 10^{10} cm^{-2}, four orders of magnitude higher than in conventional ion beam targets, was achieved. This

technique increases tremendously the number of ionic species accessible to PI experiments. In this work two approaches have been demonstrated, useful for both low and high ionization threshold energies respectively. Firstly, a measurement consisting of several phases separating target ion production and photoion detection in time was applied for N^{3+}. This cyclic procedure also enabled efficient depopulation of metastable states. With an ionization potential of only 77 eV, N^{3+} is close to the lower limit of applicability of this technique. Results in this energy range, with a typical accuracy of 0.05 eV, were compared to those from the established merged beam method, which show excellent agreement. Secondly, Ar^{8+}, a case of high ionization potential (422 eV), was measured in a continuous mode giving unprecedented access to ions in high charge states and with high ionization potential. This will enable investigations of long isoelectronic and isonuclear sequences and give interesting insight into electron–electron correlations.

The measured PI values are compared to our extended full relativistic MCDF calculations. The theoretical results compare well with the measurements, i.e. within 0.3 eV for the resonance positions. Highly charged ions at higher Z values will in particular benefit from these calculations.

As strong XUV and x-ray absorption lines due to PI of HCIs have recently been observed in astrophysical spectra, and identification of these structures still has to rely almost exclusively on calculations, the present investigations constitute a first step towards better benchmarking of those models. These results together with those of [29, 30, 62] form a strong case for the installation of EBITs at synchrotrons and free-electron lasers, since astrophysics, plasma physics and atomic structure theory can all profit from the detailed studies now becoming possible.

Acknowledgments

References

[1] Cunto W, Mendoza C, Ochsenbein F and Zeippen C J 1993 *Astron. Astrophys.* **275L** 5C
[2] Hummer D G, Berrington K A and Eissner W *et al* 1993 *Astron. Astrophys.* **279** 298H
[3] Johansson S, Derkatch A and Donnelly M P *et al* 2002 *Phys. Scr.* T **100** 71
[4] Holczer T, Behar E and Kaspi S 2005 *Astrophys. J.* **632** 788
[5] Cen R and Ostriker J P 1999 *Astrophys. J.* **514** 1
[6] Savage B D, Sembach K R, Tripp T M and Richter P 2002 *Astrophys. J.* **564** 631
[7] Fang T, Marshall H L, Lee J C, Davis D S and Canizares C R 2002 *Astrophys. J. Lett.* **572** L127
[8] Wakker B P, Savage B D and Sembach K R *et al* 2003 *Astrophys. J. Suppl. Ser.* **146** 1
[9] Savage B D, Sembach K R and Wakker B P *et al* 2003 *Astrophys. J. Suppl. Ser.* **146** 125
[10] Sembach K R, Wakker B P and Savage B D *et al* 2003 *Astrophys. J. Suppl. Ser.* **146** 165
[11] Danforth C W and Shull J M 2005 *Astrophys. J.* **624** 555
[12] Nicastro F, Mathur S and Elvis M *et al* 2005 *Astrophys. J.* **629** 700
[13] Nicastro F, Mathur S and Elvis M *et al* 2005 *Nature* **433** 495
[14] Brandau C, Kozhuharov C and Müller A 2003 *Phys. Rev. Lett.* **91** 073202
[15] Müller A, Schippers S and Aguilar A *et al* 2003 *AIP Conf. Proc.* **680** 191
[16] Badnell N R 2006 *J. Phys. B: At. Mol. Opt. Phys.* **39** 4825
[17] Orban I, Lindroth E, Glans P and Schuch R 2007 *J. Phys. B: At. Mol. Opt. Phys.* **40** 1063
[18] Levine A, Marrs R E and Schmieder R W 1985 *Nucl. Instrum. Methods* A **237** 429
[19] Levine A, Marrs R E and Bradsley J N 1989 *Nucl. Instrum. Methods* B **43** 431
[20] Knapp D A, Marrs R E, Elliott S R, Magee E W and Zasadzinski R 1993 *Nucl. Instrum. Methods* A **334** 305
[21] Marrs R E, Beiersdorfer P and Schneider D 1994 *Phys. Today* **47** 27
[22] Crespo López-Urrutia J R, Bapat B, Draganic I, Werdich A and Ullrich J 2001 *Phys. Scr.* **T92** 110
[23] Wiersma R P C, Schaye J and Smith B D 2009 *Mon. Not. R. Astron. Soc.* **393** 99
[24] Müller A, Schippers S and Phaneuf R A *et al* 2007 *J. Phys. Conf. Ser.* **58** 383
[25] Bizau J-M 2009 private communication
[26] Schippers S 2009 private communication
[27] Kravis S D, Church D A and Johnson B M *et al* 1991 *Phys. Rev. Lett.* **66** 2956
[28] Thissen R, Bizau J-M and Blancard C *et al* 2008 *Phys. Rev. Lett.* **100** 223001
[29] Simon M C, Schwarz M and Schmitt B L *et al* 2009 *J. Phys: Conf. Ser.* **194** 012009
[30] Simon M C, Crespo López-Urrutia J R and Beilmann C *et al* 2009 *Phys. Rev. Lett.* submitted
[31] Bizau J-M, Esteva J-M and Cubaynes D *et al* 2000 *Phys. Rev. Lett.* **84** 435
[32] Bizau J-M, Cubaynes D and Esteva J-M *et al* 2001 *Phys. Rev. Lett.* **87** 273002
[33] Hassan N E, Bizau J-M and Blancard C *et al* 2009 *Phys. Rev.* A **79** 033415
[34] Aguilar A, Gillaspy J D and Gribakin G F *et al* 2006 *Phys. Rev.* A **73** 032717
[35] Habibi M, Esteves D and Aguilar A *et al* 2009 *J. Phys: Conf. Ser.* **194** 022089
[36] Kjeldsen H 2006 *J. Phys. B: At. Mol. Opt. Phys.* **39** R325
[37] West J B 2001 *J. Phys. B: At. Mol. Opt. Phys.* **34** R45
[38] Winhart G, Eidmann K, Iglesias C A and Bar-Shalom A 1996 *Phys. Rev.* E **53** R1332
[39] Remington B A, Drake R P and Ryutov D D 2006 *Rev. Mod. Phys.* **78** 755
[40] Foord M E, Heeter R F and van Hoof P A M *et al* 2004 *Phys. Rev. Lett.* **93** 055002
[41] Bailey J E, Rochau G A and Iglesias C A *et al* 2007 *Phys. Rev. Lett.* **99** 265002
[42] Heeter R F, Hansen S B and Fournier K B *et al* 2007 *Phys. Rev. Lett.* **99** 195001

J. Phys. B: At. Mol. Opt. Phys. **43** (2010) 065003

M C Simon *et al*

[43] Greiche A, Liang Y and Marchuk O *et al* 2009 *Plasma Phys. Control. Fusion* **51** 032001

[44] von Hellermann M, Bertschinger G and Biel W *et al* 2005 *Phys. Scr.* **T120** 19

[45] May M, Finkenthal M and Moos H *et al* 2001 *Phys. Rev.* E **64** 036406/1

[46] Church D A, Jones K W, Johnson B M, Meron M and Sellin I A 1984 *J. Phys. B: At. Mol. Phys.* **17** L401

[47] Kravis S, Oura M, Awaya Y, Okuno K and Kimura M 1994 *Rev. Sci. Instrum.* **65** 1066

[48] Oure M, Kravis S and Koizumi T *et al* 1994 *Nucl. Instrum. Methods* B **86** 190

[49] Kravis S D, Watanabe N and Awaya Y *et al* 1997 *Phys. Scr.* **T71** 121

[50] Schulz K, Kaindl G and Domke M *et al* 1996 *Phys. Rev. Lett.* **77** 3086

[51] Chakraborty H S, Gray A and Costello J T *et al* 1999 *Phys. Rev. Lett.* **83** 2151

[52] Kennedy E T, Costello J T and Gray A *et al* 1999 *J. Electron Spectrosc. Relat. Phenom.* **103** 161

[53] Bizau J M, Mosnier J P and Kennedy E T *et al* 2009 *Phys. Rev.* A **79** 033407

[54] Maeda K, Ueda K and Ito K 1993 *J. Phys. B: At. Mol. Opt. Phys.* **26** 1541

[55] Wang J C, Lu M and Esteves D *et al* 2007 *Phys. Rev.* A **75** 062712

[56] Wright J D, Morgan T J and Li L *et al* 2008 *Phys. Rev.* A **77** 062512

[57] Lu X and Currell F J 2009 *Phys. Rev. ST Accel. Beams* **12** 014401

[58] Penetrante B M, Bardsley J N, DeWitt D, Clark M and Schneider D 1991 *Phys. Rev.* A **43** 4861

[59] Penetrante B M, Bardsley J N, Levine M A, Knapp D A and Marrs R E 1991 *Phys. Rev.* A **43** 4873

[60] Liang G Y, Baumann T M and Crespo López-Urrutia J R *et al* 2009 *Astrophys. J.* **696** 2275

[61] Liang G Y, Crespo López-Urrutia J R and Baumann T M *et al* 2009 *Astrophys. J.* **702** 838

[62] Epp S W, Crespo López-Urrutia J R and Brenner G *et al* 2007 *Phys. Rev. Lett.* **98** 183001

[63] Martins M, Kaindl G and Schwentner N 1999 *J. Electron Spectrosc. Relat. Phenom.* **101** 965

[64] Sawhney K, Senf F and Gudat W 2001 *Nucl. Instrum. Methods* A **467** 466

[65] Follath R *et al* 2004 *AIP Conf. Proc.* **708** 348

[66] Follath R and Senf F 1997 *Nucl. Instrum. Methods* A **390** 388

[67] Beiersdorfer P, Schweikhard L, Crespo López-Urrutia J R and Widmann K 1996 *Rev. Sci. Instrum.* **67** 3818

[68] Bizau J M, Champeaux J P and Cubaynes D *et al* 2005 *Astron. Astrophys.* **439** 387

[69] Jones K W, Johnson B M and Meron M 1983 *Phys. Lett.* A **97** 377

[70] Fritzsche S, Aksela H, Dong C Z, Heinäsmäki S and Sienkiewicz J E 2003 *Nucl. Instrum. Methods* B **205** 93

[71] Harman Z, Tupitsyn I I and Artemyev A N *et al* 2006 *Phys. Rev.* A **73** 052711

[72] Zimmermann M, Grün N and Scheid W 1997 *J. Phys. B: At. Mol. Opt. Phys.* **30** 5259

[73] Fano U 1961 *Phys. Rev.* **124** 1866

[74] Grant I P 1970 *Adv. Phys.* **19** 747

[75] Desclaux J P, Mayers D F and O'Brien F 1971 *J. Phys. B: At. Mol. Phys.* **4** 631

[76] Zimmerer P, Grün N and Scheid W 1990 *Phys. Lett.* A **148** 457

[77] Nahar S N and Pradhan A K 1997 *Astrophys. J. Supp. Ser.* **111** 339

[78] Nahar S N 2009 *NORAD* www.astronomy.ohio-state.edu/~nahar/

[79] Müller A, Schippers S and Phaneuf R A *et al* 2007 *25th ICPEAC (Freiburg, Germany), conference program* p 121 (Fr021)

[80] Tully J A, Seaton M J and Berrington K A 1990 *J. Phys. B: At. Mol. Opt. Phys.* **23** 3811

[81] Wiese W L, Fuhr J R and Deters T M 1996 *J. Phys. Chem. Ref. Data* **7** 267

[82] Cowan R D 1981 *Theory of Atomic Structure and Spectra* (Berkeley, CA: University of California Press)

[83] Los Alamos Atomic Physics Codes: http://aphysics2.lanl.gov/tempweb/lanl/

[84] Liang L, Chao Z and Xie Z-X 2009 *Opt. Commun.* **282** 558